Asociación Argentina de Astronomía
Third La Plata International School on Astronomy and Geophysics:
Chaos, diffusion and non–integrability in Hamiltonian Systems
Applications to Astronomy , 2012
P. M. Cincotta, C. M. Giordano & C. Efthymiopoulos, eds.

ORAL COMMUNICATION

Diffusion measurements in a 3DoF Hamiltonian flow.

M. F. Mestre [1,2], P.M. Cincotta [1,2], C.M. Giordano[1,2]

(1) Instituto de Astrofísica de La Plata (CONICET)
(2) Grupo de Caos en Sistemas Hamiltonianos
Facultad de Ciencias Astronómicas y Geofísicas - UNLP
Paseo del Bosque, B1900FWA La Plata, Argentina

Abstract. We present measurements of diffusion phenomenae in the phase space of a three degree of freedom *quasi*–integrable Hamiltonian flow. By tracking the evolution of the variance of ensembles of test particles, we characterize the diffusion as basically anomalous. We find a time range in which it can be considered as a subdiffusion process and other in which it can be considered as a normal diffusion process. In the former case we fit Hurst exponents and in the latter case we compute diffusion coefficients based on the rate of growth of the variances.

1. Introduction

In this contribution we will study numerically a diffusion process that takes place in the stochastic layer of a non–linear resonance of a particular *quasi*–integrable three degree of freedom (3DoF) Hamiltonian flow. We will focus in a resonant region of multiplicity one; i.e. isolated resonance region.

The experiments are based on evolving ensembles of test particles and measuring some statistical quantities. For the values of total energy and resonant action that will be considered here, we will have examples of subdiffusion in both *overlapping* and *non–overlapping* local regimes, depending on the value of the perturbation parameter. We will also identify time ranges in which there is a diffusion behaviour approximately normal that will allow us to compute standard diffusion coefficients.

The structure of the article is as follows.

In subsection 1.1. we present a one degree of freedom (1DoF) quartic oscillator and give its solution and its action–angle variables. In subsection 1.2. we present the 3DoF *quasi*–integrable Hamiltonian flow whose diffusion properties we will study throughout this work. The integrable part of this Hamiltonian consists in three independent 1DoF quartic oscillators. In subsection 1.3. we specify a linear canonical transformation that allows to measure diffusion in a new set of *quasi*–integrals which are geometrically easier to analyse. In subsection 1.4. we define some statistical quantities based on ensemble averages. In subsection 1.5. we explain briefly the numerical integrators used herein.

In section 2. we present the geometric situation of the chosen resonant action, the guiding resonance and its neighbourhood. In section 3. we describe some numerical experiments done with ensembles of test particles, analysing the

functional form of the time evolution of some statistical quantities. We compute Hurst exponents and diffusion coefficients for different values of the perturbation parameter. Finally, in section 4. we give a summary of the obtained results.

1.1. The quartic oscillator

The *quartic oscillator* is given by the Hamiltonian

$$\tilde{H}(v,x) = \frac{v^2}{2} + \frac{x^4}{4}, \tag{1}$$

where v and x are real variables. The associated system of differential equations is given by:

$$\frac{dv}{dt} = -x^3, \qquad \frac{dx}{dt} = v. \tag{2}$$

Let h be the total energy and let a be the oscillation amplitude. Then,

$$h = \tilde{H}(0,a) = \frac{a^4}{4}$$

and Eqs. (2) can be rewritten as

$$\left(\frac{dx}{dt}\right)^2 = \frac{1}{2}(a^4 - x^4),$$

whose solution can be expressed in terms of the *Jacobi elliptic cosine* (cn) *of modulus* $k = 1/\sqrt{2}$:

$$x(t) = a\ \mathrm{cn}(at,k) = a\ \mathrm{cn}(at,\ 1/\sqrt{2}).$$

Using the Fourier series development of the Jacobi elliptic cosine given by Gradshtyn & Ryzhik (1980), we have that (Chirikov 1979):

$$x(t) = a\frac{\sqrt{2}\pi}{K_0}\sum_{n=1}^{\infty}\frac{1}{\cosh\left((n-1/2)\pi\right)}\cos\left((2n-1)\frac{\pi a t}{2K_0}\right),$$

where $K_0 \equiv K(1/\sqrt{2})$ denotes the *complete elliptic integral of the first kind.*

Introducing the following constants:

$$\beta \equiv \frac{\pi}{2K_0} \approx 0.847213084793979, \qquad \alpha_n \equiv \frac{1}{\cosh\left((n-1/2)\pi\right)} \qquad \text{and} \quad \omega \equiv \beta a, \tag{3}$$

we have that

$$x(t) = 2^{3/2}\omega\sum_{n=1}^{\infty}\alpha_n\cos\left((2n-1)\omega t\right).$$

This equation implies that the quantity ω is the fundamental frequency of the motion.

The α_n coefficients satisfy:

$$\frac{\alpha_{n+1}}{\alpha_n} \approx \frac{1}{23} \qquad \text{for n} \geq 2 \qquad \text{and} \qquad \alpha_1 \approx 0.4.$$

Taking into account the previous relation between a and h and Eq. (3), we obtain the dependence between the latter and ω:

$$\omega = \sqrt{2}\beta h^{1/4}. \tag{4}$$

Due to the fact that the Hamiltonian equations in action–angle variables (I, θ) imply that $\omega(I) = \frac{\partial H(I)}{\partial I}$, it is possible to integrate Eq. (4), obtaining the relation between the action and the energy of the system.

$$h = AI^{4/3}, \qquad \text{or equivalently} \quad I = \left(\frac{h}{A}\right)^{3/4},$$

where $A \equiv (3\beta/2\sqrt{2})^{4/3} \approx 0.867145326484821$.

Let us mention that the dependence of the frequency on the action is given by:

$$\omega(I) = \frac{4}{3}AI^{1/3} \tag{5}$$

The cartesian coordinate can be expressed in terms of the action–angle variables of the system, in the fashion:

$$\begin{aligned} x(I,\theta) =& (3\beta I)^{1/3}\mathrm{cn}\left(\frac{\theta}{\beta}, \frac{1}{\sqrt{2}}\right) \\ v(I,\theta) =& \varrho\sqrt{2\left(AI^{4/3} - \frac{1}{4}[x(I,\theta)]^4\right)}, \end{aligned} \tag{6}$$

where ϱ stands for the sign of v and its dependence on the angle is given by:

$$\varrho \equiv \begin{cases} 1 & \text{if } 0 \leq \theta < \pi, \\ -1 & \text{if } \pi \leq \theta < 2\pi. \end{cases} \tag{7}$$

Besides, the inverse transformation[1] of Eqs. (6)(7) is given by:

$$I(v,x) = \left[\frac{1}{A}\left(\frac{1}{2}v^2 + \frac{1}{4}x^4\right)\right]^{3/4}, \tag{8}$$

$$\theta(v,x) = \begin{cases} \beta\ \mathrm{cn}^{-1}\left(\frac{x}{[3\beta\ I(v,x)]^{1/3}}, \frac{1}{\sqrt{2}}\right) & \text{if } v \geq 0, \\ 2\pi - \beta\ \mathrm{cn}^{-1}\left(\frac{x}{[3\beta\ I(v,x)]^{1/3}}, \frac{1}{\sqrt{2}}\right) & \text{if } v < 0. \end{cases} \tag{9}$$

[1]The angle is not well defined when the action is zero.

1.2. The 3DoF Hamiltonian system

Now we will introduce the 3DoF Hamiltonian flow whose diffusion properties we would like to investigate. The system consists of three quartic oscillators coupled by a non–integrable perturbation. In cartesian variables, $\boldsymbol{x} = (x_1, x_2, x_3)$ and $\boldsymbol{v} = (v_1, v_2, v_3)$, the Hamiltonian is given by:

$$\tilde{H}(\boldsymbol{v}, \boldsymbol{x}) = \tilde{H}_0(\boldsymbol{v}, \boldsymbol{x}) + \varepsilon \tilde{V}(\boldsymbol{x}), \tag{10}$$

with

$$\begin{aligned} \tilde{H}_0(\boldsymbol{v}, \boldsymbol{x}) &= \frac{1}{2}(v_1^2 + v_2^2 + v_3^2) + \frac{1}{4}(x_1^4 + x_2^4 + x_3^4), \\ \tilde{V}(\boldsymbol{x}) &= x_1^2(x_2 + x_3); \end{aligned} \tag{11}$$

where ε is a *perturbation parameter* that controls the strength of the coupling. For a null value of ε one obtains the integrable Hamiltonian of three independent quartic oscillators. By means of Eqs. (6)(7) the cartesian variables can be expressed in terms of their action–angle counterparts:

$$x_j(I_j, \theta_j) = (3\beta I_j)^{1/3} \mathrm{cn}\left(\frac{\theta_\mathrm{j}}{\beta}, \frac{1}{\sqrt{2}}\right), \qquad \text{for} \quad \mathrm{j} = 1, 2, 3$$

Moreover, according to Eq. (5) the frequency vector is given by:

$$\boldsymbol{\omega}(\boldsymbol{I}) \equiv \big(\omega_1(I_1), \omega_2(I_2), \omega_3(I_3)\big) = \frac{4}{3} A(I_1^{1/3}, I_2^{1/3}, I_3^{1/3}).$$

On the other hand, for $\varepsilon \neq 0$, only one globally conserved quantity exists, the total energy $\tilde{H}(\boldsymbol{v}, \boldsymbol{x}) = \tilde{H}(\boldsymbol{v}(0), \boldsymbol{x}(0)) \equiv h$. In terms of the action–angle variables (of the unperturbed Hamiltonian) the full Hamiltonian, given by Eqs. (10)(11), can be rewritten as:

$$H(\boldsymbol{I}, \boldsymbol{\theta}) = H_0(\boldsymbol{I}) + \varepsilon V(\boldsymbol{I}, \boldsymbol{\theta}), \tag{12}$$

with

$$\begin{aligned} H_0(\boldsymbol{I}) \;\; &= A({I_1}^{4/3} + I_2^{4/3} + I_3^{4/3}), \\ V(\boldsymbol{I}, \boldsymbol{\theta}) &= 3\beta I_1^{2/3} \mathrm{cn}^2\left(\frac{\theta_1}{\beta}, \frac{1}{\sqrt{2}}\right) \left[\mathrm{I}_2^{1/3} \mathrm{cn}\left(\frac{\theta_2}{\beta}, \frac{1}{\sqrt{2}}\right) + \mathrm{I}_3^{1/3} \mathrm{cn}\left(\frac{\theta_3}{\beta}, \frac{1}{\sqrt{2}}\right)\right]. \end{aligned} \tag{13}$$

This Hamiltonian system has been previously studied by Cincotta *et al.* (2003), Giordano and Cincotta (2004) and Mestre *et al.* (2009). Herein we adopt a fixed value of the total energy:

$$h \equiv 0.485254297422903 \quad \approx 1/4\beta^4, \tag{14}$$

which corresponds to a *characteristic period*[2] of the system very close to 2π.

[2]It refers to the period of the x_2, x_3-axial periodic orbits, which remain stable for every ε.

1.3. A natural base for the action space

Chirikov (1979) introduces a linear change of variables that exploits the resonant geometry in the neighbourhood of the initial conditions that belong to the stochastic layer of an isolated resonance. In this part, we present a 3DoF version of Chirikov's change of variables.

Let $\boldsymbol{m}_g$ be a harmonic vector whose contribution in the Fourier series of V is not zero. Then, Eqs. (12)(13) can be recast as:

$$H(\boldsymbol{I},\boldsymbol{\theta}) = H_0(\boldsymbol{I}) + \varepsilon V_{\boldsymbol{m}_g}(\boldsymbol{I})\cos(\boldsymbol{m}_g\cdot\theta) + \varepsilon V(\boldsymbol{I},\boldsymbol{\theta})$$

$$V(\boldsymbol{I},\boldsymbol{\theta}) = \sum_{\boldsymbol{m}\neq\boldsymbol{m}_g} V_{\boldsymbol{m}}(\boldsymbol{I})\cos(\boldsymbol{m}\cdot\theta).$$

Now we assume that the term associated to $\boldsymbol{m}_g$ turns on a non–linear resonance of H_0, along which we want to measure the diffusion. This resonance is usually called the *guiding resonance*. Let $\boldsymbol{I}^r$ be the resonant action in whose neighbourhood we want to perform these measurements. Besides, let $\boldsymbol{\omega}^r \equiv \boldsymbol{\omega}(\boldsymbol{I}^r)$ be the concomitant frequency and let $\boldsymbol{n}_g$ be a vector normal to the resonant surface, called $\mathcal{S}_g$. This last vector can be computed by

$$\boldsymbol{n}_g = \left[\frac{\partial}{\partial \boldsymbol{I}}(\boldsymbol{m}\cdot\boldsymbol{\omega}(\boldsymbol{I}))\right]_{|\boldsymbol{I}=\boldsymbol{I}^r} \tag{15}$$

Moreover, we define the vectors:

$$\begin{aligned}\boldsymbol{\mu}_1 &= \boldsymbol{m}_g,\\ \boldsymbol{\mu}_2 &= \boldsymbol{\omega}^r/|\boldsymbol{\omega}^r|\\ \boldsymbol{\mu}_3 &= (\boldsymbol{n}_g\wedge\boldsymbol{\omega}^r)/|\boldsymbol{n}_g\wedge\boldsymbol{\omega}^r|,\end{aligned} \tag{16}$$

and the matrix $\Upsilon \in \mathbb{R}^{3\times 3}$, whose $i-$th row is the vector $\boldsymbol{\mu}_i$. These vectors are linearly independent *iff* $\boldsymbol{m}_g$ is not perpendicular to $\boldsymbol{n}_g$. A way to ensure this geometrical condition is to assume that the unperturbed Hamitonian satisfies a convexity condition which can be stated as follows in terms of the *Hessian* matrix, C, of H_0:

$$[C(\boldsymbol{I})\boldsymbol{u}]\cdot\boldsymbol{u} \neq \boldsymbol{0} \qquad \forall \boldsymbol{u}\in\mathbb{R}^3\setminus\boldsymbol{0}.$$

Then, our Hamiltonian is convex because it satisfies:

$$[C(\boldsymbol{I})\boldsymbol{u}]\cdot\boldsymbol{u} = \frac{4}{9}A\left(\frac{u_1^2}{I_1^{2/3}} + \frac{u_2^2}{I_2^{2/3}} + \frac{u_3^2}{I_3^{2/3}}\right) > 0 \qquad \forall \boldsymbol{u}\in\mathbb{R}^3\setminus\boldsymbol{0}.$$

Let F be a generatrix function given by:

$$F(\boldsymbol{p},\boldsymbol{\theta}) \equiv \sum_{j=1}^{3}\left(I_j^r + \sum_{k=1}^{3} p_k\Upsilon_{kj}\right)\theta_j.$$

Then, the canonical transformation

$$\psi_i = \frac{\partial F}{\partial p_i} = \sum_k \Upsilon_{ik}\theta_k,$$
$$I_i = \frac{\partial F}{\partial \theta_i} = I_i^r + \sum_k p_k \Upsilon_{ki},$$

can be rewritten explicitly as:

$$\begin{aligned} \psi_i &= \frac{\partial F}{\partial p_i} = \sum_k \Upsilon_{ik}\theta_k, \\ p_i &= \sum_k \Upsilon_{ik}^{-T}(I_k - I_k^r), \end{aligned} \tag{17}$$

where $\Upsilon^{-T} \equiv (\Upsilon^T)^{-1}$ denotes the inverse matrix of Υ's transpose. This transformation consists of a translation of the origin to the resonant action, followed by a change of base in the phase space. The restriction of the new base to the action space, that will be called *Chirikov's base*, is made up of the $\boldsymbol{\mu}_i$ vectors. As $\boldsymbol{\mu}_1$ is equal to the resonant harmonic, its conjugate angle, $\psi_1 \equiv \boldsymbol{m}_g \cdot \boldsymbol{\theta}$, is the resonant phase of the simple pendulum that models (approximately) the dynamics in this single resonance region, $\boldsymbol{\mu}_2$ is a versor normal to the unperturbed energy surface, $\mathcal{I}_0$, and $\boldsymbol{\mu}_3$ is a versor that is orthogonal to both n_g and $\boldsymbol{\mu}_2$. In other words, it is tangent to the curve formed by the intersection between the surfaces $\mathcal{S}_g$ and $\mathcal{I}_0$, at the point $\boldsymbol{I}^r$.

Eq. (17) can be rewritten in matrix shape as follows:

$$\boldsymbol{\psi} = \Upsilon\boldsymbol{\theta},$$
$$\boldsymbol{p} = \Upsilon^{-T}(\boldsymbol{I} - \boldsymbol{I}^r).$$

Although the variables $\boldsymbol{p}$ and $\boldsymbol{\psi}$ are not necessarily action–angle variables of H_0, it does happen that the components of $\boldsymbol{p}$ are conserved quantities under the unperturbed flow. According to the definition of Υ, the columns of Υ^T correspond to Chirikov's base and, therefore, Υ^T is the matrix that transforms from this new base towards the canonical one. For this reason, p_k $(k = 1, 2, 3)$ are the components of the vector $\boldsymbol{I} - \boldsymbol{I}^r$ in Chirikov's base, whose geometrical importance is as follows (see Cincotta 2002):

- p_1 measures the displacement of $\boldsymbol{I}$ respect to $\boldsymbol{I}^r$, in the direction of the resonant vector.
- p_2 measures the displacement in the direction perpendicular to $\mathcal{I}_0$.
- p_3 measures the displacement along the resonance; i.e. in the direction in which Arnold diffusion (see below) occurs.

1.4. Statistical quantities and diffusion

We will measure some statistical quantities of the integrals of the unperturbed flow, $\boldsymbol{p}$, defined in the previous subsection. The statistical quantities will be ensemble averages computed numerically over a finite number, N_p, of test particles. This averaging operation will be symbolized by $\langle\cdot\rangle$. The initial conditions of these test particles will be *quasi*–identically chosen in the action space, all of them having the same total energy.

Let $p_j(t,i)$ be the value of the j–th component of the vector $\boldsymbol{p}$, at the time t, associated to the i–th particle. Thus, the (instantaneous) *mean* value of this component is given by:

$$\mu_j(t) \equiv \langle p_j(t) \rangle \equiv \frac{1}{N_p} \sum_{i=1}^{N_p} p_j(t,i),$$

and the corresponding *variance* is:

$$\sigma_j^2(t) \equiv \langle (p_j(t) - \mu_j(t))^2 \rangle \equiv \frac{1}{N_p} \sum_{i=1}^{N_p} (p_j(t,i) - \mu_j(t))^2. \tag{18}$$

Other average quantity that will be used is the *mean square displacement* (MSD):

$$\gamma_j^2(t) \equiv \langle (p_j(t) - p_j(0))^2 \rangle \equiv \frac{1}{N_p} \sum_{i=1}^{N_p} (p_j(t,i) - p_j(0,i))^2, \tag{19}$$

There is not a universal definition of the term *diffusion*. The characterization of this concept depends on many factors: the research area, the system under study, the mathematical tools and the variables used, for example. When working with non–integrable deterministic systems, the term *chaotic diffusion* is usually adopted. In this article, we will say that an ensemble *diffuses* whenever the evolution of its variance performs a non–negligible secular growth in time, allowing this quantity to have oscillations.

In Nekhoroshev (1977), Chirikov (1979), Guzzo *et al.* (2005) and Efthymiopoulos (2008) the concept of *Arnold diffusion* is understood as the one that takes place along the *Arnold web*[3] of a system that satisfies simultaneously the hypothesis of both KAM (Arnold 1989) and Nekhoroshev (Nekhoroshev 1977, see Morbidelli 2006 for a relaxed version) theorems. In this sense, Lega *et al.* (2003), Guzzo *et al.* (2005) and Froeschlé *et al.* (2005) show evidence of Arnold diffusion.

The *standard deviation* is the square root of the variance. This two quantities are sensitive to the degree of diffusion of the ensemble with respect to the geometrical centre ($\boldsymbol{\mu}$) but are not influenced by it. On the other hand, the MSD depends both on the diffusion of the ensemble and on the dynamics of the geometrical centre.

We will consider that a dynamical variable performs a *normal diffusion* if its variance is a linear function of time. Other close definition, generally adopted in the literature, is that *normal diffusion* implies that the MSD behaves linearly with time. One of the paradigmatic systems which present normal diffusion belongs to the class of *stochastic processes*[4], is called *Wiener process* or *Brownian motion* (BM) and was studied by Einstein (1956) among others.

---

[3]Arnold web is the intersection of all the perturbed resonant surfaces with the isoenergetic manifold given by $H(\boldsymbol{I}, \boldsymbol{\theta}) = h$.

[4]The definition of *stochastic process* can be found at Gardiner (2004) or Arnold (1973)

In the case of normal diffusion, it is possible to define a *diffusion coefficient*, denoted $\mathcal{D}_\sigma$, which in this work will be strictly associated to σ_3^2, by the following formula:

$$\mathcal{D}_\sigma \equiv \frac{\sigma_3^2(t) - \sigma_3^2(t_0)}{2(t - t_0)}. \tag{20}$$

Due to inhomogeneities of phase space, $\mathcal{D}_\sigma$ is significant as long as most of the ensemble particles are inside a region small enough so that the diffusion properties are similar all over it. Sometimes it is possible to obtain locally normal behaviours, by limiting the size of the time interval, $|t - t_0|$, in order that the majority of the ensemble stays close to its initial region of action space. This approach, of associating a diffusion coefficient to a neighbourhood of a given initial action, has been adopted in many works (Novaković *et al.* 2010, Todorović *et al.* 2008, Lega *et al.* 2003, Froeschlé *et al.* 2005, Bazzani & Mais 1998, Bazzani *et al.* 1997, Siboni *et al.* 1994, Bountis & Kollmann (1994), for instance). In particular, Lega *et al.* 2003 compute numerically a kind of diffusion coefficient, $\mathcal{D}_\gamma$, related with the MSD, for different values of ε. They detect that the diffusion coefficient goes to zero faster than any power law: $\mathcal{D}_\gamma(\varepsilon) \propto \varepsilon^a$, for any constant a. They also mention that this is compatible with an exponential law: $\mathcal{D}_\gamma(\varepsilon) \propto \exp(-1/\varepsilon^b)$, for some constant b.

Normal diffusion has been widely applied to model dynamical problems in Astronomy, specially in Solar System dynamics.

Diffusion can also be *anomalous*. Mandelbrot & van Ness (1968) introduce, for the first time, the *fractional Brownian motion* (FBM), in terms of a particular *stochastic integral*[5] of the BM.

Any FBM has a standard deviation whose time dependence is given by:

$$\sigma_\eta(t) \propto t^\eta, \tag{21}$$

where η is called the *Hurst exponent*.

This uniparametric family of stochastic processes can be classified in three groups, depending on the value of the exponent:

- *subdiffusive* if $0 < \eta < \frac{1}{2}$,
- *normal* (BM) if $\eta = \frac{1}{2}$,
- *superdiffusive* if $\frac{1}{2} < \eta < 1$.

Cordeiro & Mendes de Souza (2005) and Cordeiro (2006) model diffusion properties, in Solar System resonance domains, with an approach based on FBM.

There are many other types of anomalous diffusion processes. Chechkin *et al.* (2008) presents an introduction to *Lévy flights*. Metzler *et al.* (2007) analyses this process together with *Lévy walks*, subdiffusion processes and fractional *Fokker-Planck* equations. Zaslavsky (2002) revises many fractional stochastic models and their connection with dynamical models, phase space topology and other characteristics of chaos, as the *Poincaré recurrences* and the *sticky domains*.

[5]The definition of *stochastic integral* can be found at Gardiner (2004) or Arnold (1973)

In this work we will present numerical evidence of subdiffusion, that occurs during a rather large time interval. Nevertheless, the full diffusion behaviour along a single resonance of this Hamiltonian system is much more complex than the one of a FBM.

1.5. The numerical integrators

The numerical integrator used in this article to compute the trayectories with which the statistical quantities where performed is a symplectic integrator elaborated by E. Teloy, Freiburg, as mentioned in Schlier & Seiter (2000).

This subroutine consists of five integrators, two of 6^{th} order and three of 8^{th} order, called S6a, S6b, S8a, S8b and S8c, respectively.

The kernel of the source code, that performs the integration of a single time step, is called *testsymp*[6]. This code contains the coefficients for the five integration schemes with 35 decimal figures, which is enough for a quadruple precision integration.

After some comparison between the five schemes, the one which better preserved energy was the *S8b*. Regarding measurement of statistical (or average) quantities any of the integrators turned out to be appropriate. The same happened when doing chromatic maps with a chaos indicator called *Smaller Alignment Index* (SALI), introduced by Skokos (2001) , where all of the schemes displayed similar resonant structures. The results presented in this article where obtained with the *S8b* method.

We made a test experiment with two different integration time steps: $\Delta t_{int} = 10^{-2}$ and $\Delta t_{int} = 10^{-1}$, obtaining agreement in the resonant structure of the SALI maps and in the general trend of statistical quantities. Then, for the sake of efficiency, we decided to use in all the experiments of this work, an integration time step of size $\Delta t_{int} = 10^{-1}$.

In this work, we also use the integrator DOPRI8 (Prince & Dormand 1981), in order to build maps of other chaos indicator called *Mean Exponential Growth Factor of Nearby Orbits* (MEGNO), introduced by Cincotta & Simó (2000). Strictly speaking, the indicator effectively used is a *cumulative running time average* of the MEGNO, denoted by $\bar{Y}$. All the integrations where done in cartesian variables.

2. The guiding resonance and its neighbourhood

Now we will characterize geometrically the phase space of the 3DoF Hamiltonian system. In particular, we will specify the guiding resonance where we want to measure diffusion. Such information will be displayed for the case of $\varepsilon = 0.02$.

According to Giordano & Cincotta (2004) the fraction of *chaotic orbits*[7] in $\mathcal{I}_0$, for this parameter value, is of a 38%, while for $\varepsilon = 0.04$ it is approximately of a 92%. Thus, the authors deduced that there is some threshold value of ε close to 0.03, above which chaotic motion prevails in phase space.

---

[6]It can be found at CPC Program Library, Queen's University of Belfast, N. Ireland.

[7]They computed $\bar{Y}$ for initial conditions distributed all over $\mathcal{I}_0$, considering as *chaotic orbits* to those with value $\bar{Y} \geq 2$.

Additionally, in Mestre *et al.* (2009), it was determined analytically, through the *overlap criterion*, that for some critical value of ε (denoted as ε_c) also close to 0.03, the total area covered by resonant regions reaches 90% of the whole area of $\mathcal{I}_0$.

Fig. 1 was built using chromatic levels of $\bar{Y}$ for initial conditions that fill $\mathcal{I}_0$. The $\bar{Y}$ values where binned in five intervals: $[1.993, 2.005]$ (red), $[2.005, 5]$ (green), $[5, 45]$ (blue), $[45, 150]$ (magenta) and $[150, 383]$ (cyan).

The integration of this orbits was done with DOPRI8 for a total time, t_T, of 3500 characteristic periods ($t_T = 3500 \times 2\pi$ time units). In the mentioned figure we can see the resonant structure in the action space, for a section of initial angles given by $\theta_i = \pi/2$ $(i = 1, 2, 3)$. Such an angle choice corresponds to null initial values of x_i $(i = 1, 2, 3)$, as it can be deduced from the canonical transformation given by Eq. (6) and from properties of the elliptic cosine. Due to this reason, it happens that $\tilde{V}(\boldsymbol{x}(0)) = \tilde{V}(\mathbf{0}) = 0$, implying that

$$\tilde{H}(\boldsymbol{v}(0), \boldsymbol{x}(0)) = \tilde{H}_0(\boldsymbol{v}(0), \mathbf{0}). \tag{22}$$

Then, the initial value of I_3 was solved from the equation $H_0(\boldsymbol{I}) = h$, using the expression:

$$I_3(0) = \left(\frac{h}{A} - I_1(0)^{4/3} - I_2(0)^{4/3} \right)^{3/4}. \tag{23}$$

In the given figure, we identify in cyan a large region of resonance overlap. Moreover, we can appreciate how the most regular initial conditions (red points) are placed in the complement of the Arnold web, being it filled by the rest of the colors associated to chaotic orbits.

Due to the fact that the SALI indicator tends exponentially to zero for chaotic orbits, we will use the decimal logarithm of this quantity and will use a cut–off criteria that consists of assigning the values $\log(\text{SALI}) = -10$ to every orbit with $\text{SALI} < 10^{-10}$.

In Fig. 2 we display a bidimensional map of this indicator, for a part of $\mathcal{I}_0$, projected onto the $[I_1, I_2]$ plane. To make this figure we have integrated a grid of 1000×1000 initial conditions that belong to the square $(I_1, I_2) \in [0.2,\ 0.4] \times [0.0,\ 0.2]$ and to the same section of initial angles than in the previous figure. For each initial condition, we have used $t_T = 10^4$ time units, which corresponds to more than 10^3 times the characteristic period of the system. The behaviour of the SALI and the color palette are such that the most chaotic orbits appear in black while the most regular ones appear in yellow.

In the given figure, we can see three wide resonances together with many other of smaller size. The nearly horizontal resonance that goes from $(I_1, I_2) \approx (0.2,\ 0.05)$ up to $(I_1, I_2) \approx (0.4,\ 0.1)$ corresponds to the resonant vector $\boldsymbol{m}_g = (2, -3, 0)$, whose direction is indicated with a green arrow. Over the chaotic layer (perturbed separatrix) of this resonance we will study diffusion, i.e. it will be the guiding resonance.

The widest resonance in the figure corresponds to the resonant vector $\boldsymbol{m} = (2, -1, -1)$ and intersects the guiding resonance approximately at $(0.22,\ 0.06)$. The third of the wide resonances correspondes to the resonant vector $\boldsymbol{m} = (2, 0, -2)$ and intersects the guiding resonance approximately at $(0.37,\ 0.10)$.

We can appreciate that for this initial angle values, the chaotic layer of the guiding resonances is thicker than the other neighbouring layers. The thickness

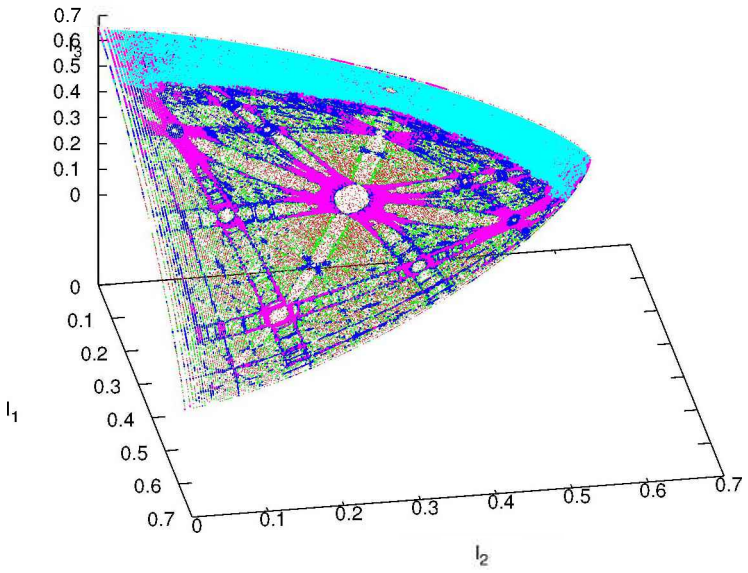

Figure 1. Cumulative running time average of the MEGNO, $\bar{Y}(t_T)$ with $t_T = 3500 \times 2\pi$, for the unperturbed energy surface in action space, using $\varepsilon = 0.02$. The association between bins and colors si given by: $[1.993, 2.005]$–red, $[2.005, 5]$–green, $[5, 45]$–blue, $[45, 150]$–magenta and $[150, 383]$–cyan.

of the stochastic layer is not constant along the resonance. For example, the neighbourhood of the point $(I_1, I_2) = (0.22,\ 0.06)$, is a resonant region of multiplicity higher than one, so that there exists a type of (unavoidable) *overlap* phenomena. The rest of the resonances perturb the separatrix in much lower ways.

3. Numerical experiments

In the following experiments we will study the diffusion for values of ε belonging to the following set:

$$\mathscr{E} = \{0.016,\ 0.018,\ 0.020,\ 0.022,\ 0.024,\ 0.026,\ 0.028,\ 0.030\}.$$

3.1. The ensembles

The selection mechanism of the initial conditions of the ensemble is based in the similarity between the phase space structure in the neighbourhood of a multiplicity-one resonance with respect to the concomitant structure of a perturbed pendulum (Chirikov 1979). This similarity will be checked graphically below.

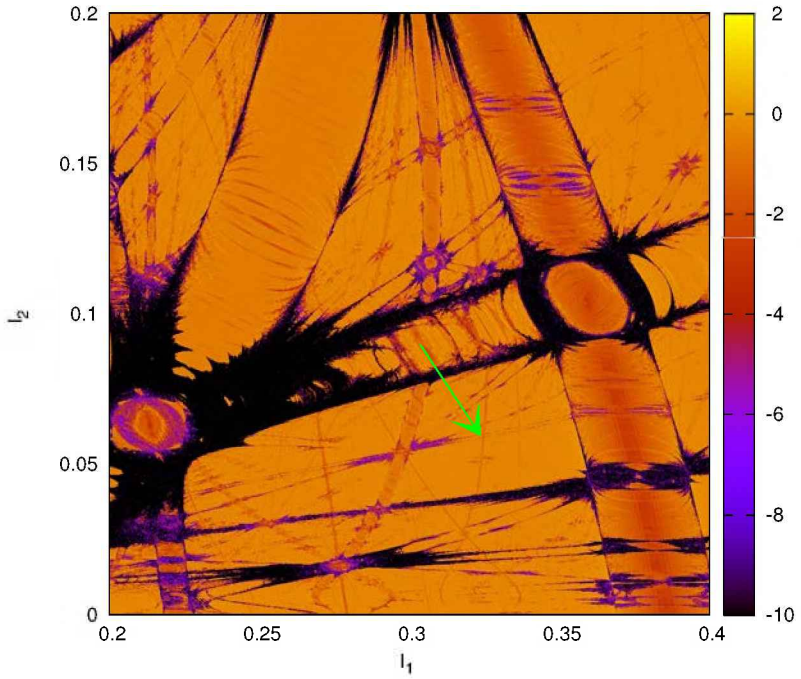

Figure 2. SALI chromatic scale in action space, for $\varepsilon = 0.02$. The color palette is such that the most chaotic orbits appear in black while the most regular ones appear in yellow. The green arrow is parallel to the vector $(2, -3)$.

With regards to the guiding resonance previously specified, and the natural change of variables given by Eq. (17), we define a particular resonant action:

$$\boldsymbol{I}^r = \begin{pmatrix} 0.303515780714549 \\ 0.089930601693199 \\ 0.420802747838120 \end{pmatrix}, \tag{24}$$

and consider the set of initial conditions that belong to a bidimensional portion of phase space parametrized by the following expression in mixed variables[8]:

$$\begin{cases} \psi_1 & \in & [0,\ 2\pi] \\ p_1 & \in & [-10^{-2},\ 10^{-2}] \end{cases} \tag{25}$$

$$\begin{cases} \theta_1 & = & \pi/2 \\ \theta_2 & = & (2\theta_1 - \psi_1)/3, \qquad mod \quad 2\pi \\ \theta_3 & = & \pi/2 \\ \boldsymbol{I} & = & \boldsymbol{I}^r + p_1 \boldsymbol{m}_g. \end{cases} \tag{26}$$

Thus chosen, the energies of this initial conditions would differ in quantities of $\mathcal{O}(\varepsilon)$, i.e. they would certainly not belong to the same energy surface,

[8]The last condition of Eq. (26) is equivalent to initial values $p_2 = p_3 = 0$.

$H(\boldsymbol{I}, \boldsymbol{\theta}) = h$. Projecting the initial conditions given by Eqs. (25)(26) onto the energy surface can be done solving I_1 as a function of I_2, I_3, $\boldsymbol{\theta}$, h and ε. We proceed in the following way. Defining

$$b \equiv \frac{\varepsilon 3\beta}{A}\mathrm{cn}^2\left(\frac{\theta_1}{\beta},\ \frac{1}{\sqrt{2}}\right)\left[\mathrm{I}_2^{1/3}\mathrm{cn}\left(\frac{\theta_2}{\beta},\ \frac{1}{\sqrt{2}}\right) + \mathrm{I}_3^{1/3}\mathrm{cn}\left(\frac{\theta_3}{\beta},\ \frac{1}{\sqrt{2}}\right)\right],$$

$$c \equiv \frac{h}{A} - (I_2^{4/3} + I_3^{4/3}),$$

and considering the Hamiltonian in action–angle variables given by Eqs. (12)(13), the energy preservation can be expressed in this way:

$$I_1^{4/3} + bI_1^{2/3} = c.$$

This equation has a real non–negative solution:

$$I_1 = \left(\frac{\sqrt{b^2+4c} - b}{2}\right)^{3/2}$$

$$\equiv H^{-1}(I_2, I_3, \theta_1, \theta_2, \theta_3; \varepsilon, h).$$

provided that $\sqrt{b^2+4c} - b \geq 0$.

For the value of h and for the ε range used in this work, such inversion is possible for all the initial conditions given by Eq. (25).

Figs. 3 and 4 display chromatic maps of $\bar{Y}(3500 \times 2\pi)$, for $\varepsilon \in \mathscr{E}$, in terms of ψ_1 and p_1, which correspond, respectively, to the resonant phase and resonant moment[9].

Taking into account the behaviour of the MEGNO and the color palette used in these pictures, it results that the most chaotic orbits are those in yellow, orange and red colors, while the most regular ones are in dark blue and black colors.

The most chaotic orbits are placed in the stochastic layer associated to the guiding resonance. We observe that, although we are working with a system with an infinite hierarchy o resonances that perturb the guiding one, the resonant phase space structure resembles fairly well the phase space structure of a periodically perturbed pendulum, as is the case in the Standard Map.

The initial conditions of the ensemble were chosen using Eq. (26), with $\psi_1 \in [0, 0.7]$ and $p_1 \in [0,\ 10^{-5}]$. In this rectangle we stablished a grid of 200 initial conditions. For all the values of $\mathscr{E}$, these ensembles belong to the concomitant stochastic layers. In particular, they are placed close to $(\psi_1, p_1) = (0, 0)$, which corresponds to the unstable equilibrium point of the pendulum model. This initial ensembles are identified in the given figures with green points.

3.2. The measurements

For $\varepsilon \in \mathscr{E}$, we integrated the orbits of the ensembles. The task of the program, before each "printing time", is given by the following steps. First, it computes

[9] As explained in subsection 1.3.

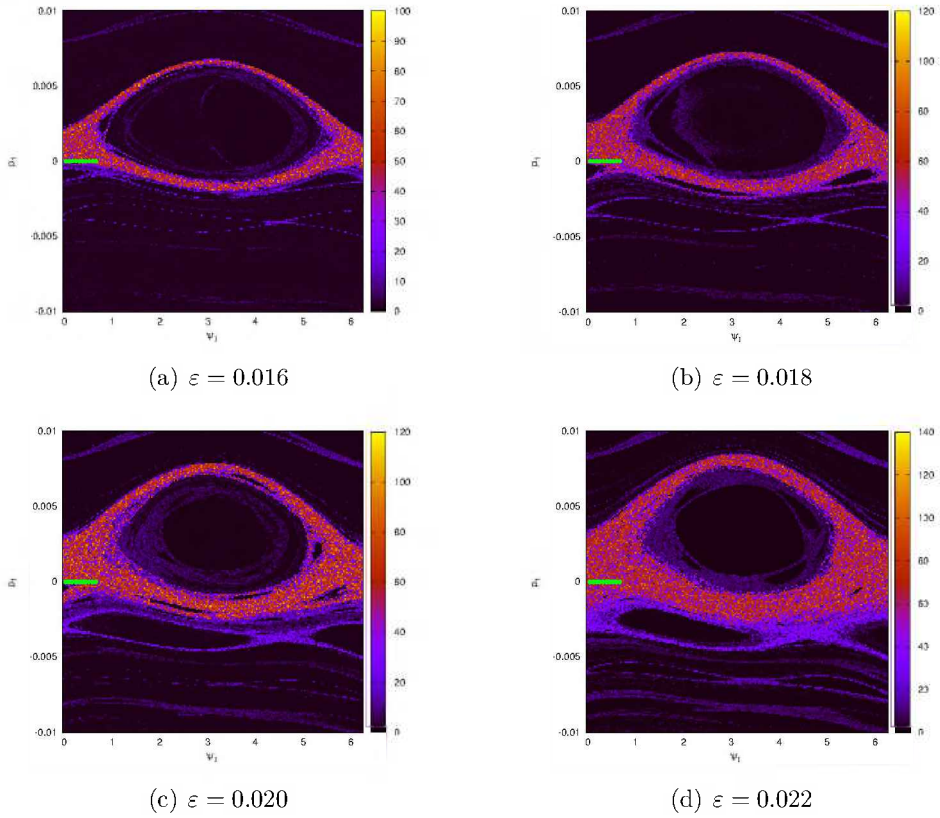

(a) $\varepsilon = 0.016$ (b) $\varepsilon = 0.018$

(c) $\varepsilon = 0.020$ (d) $\varepsilon = 0.022$

Figure 3. $\bar{Y}(3500 \times 2\pi)$, for $\varepsilon \in \{0.016,\ 0.018,\ 0.020,\ 0.022\}$, in a neighbourhood of $\boldsymbol{I}^r$ as given by Eq. (24), using pendulum variables (ψ_1, p_1). The green points identify the initial conditions of the ensembles.

the action variables using formula (8). Second, it transforms the actions to Chirikov's base (16), obtaining the values of the vector $\boldsymbol{p}$. Third, it computes the ensemble variances, σ_j^2 (18) and MSDs, γ_i^2 (19), for each one of the variables p_j $(j = 1, 2, 3)$. As the base vector $\boldsymbol{\mu}_1$ has a norm $||\boldsymbol{m}_g|| = \sqrt{13} \neq 1$, while the other two base vectors are normalized by definition, the statistical quantities associated to p_1 have been normalized. In other words, from now on, with the notation σ_1, σ_1^2, γ_1 and γ_1^2, we will be really denoting the quantities $\sqrt{13}\sigma_1$, $13\sigma_1^2$, $\sqrt{13}\gamma_1$ and $13\gamma_1^2$, respectively. These are the quantities that we would have measured if we had taken a normalized version of $\boldsymbol{\mu}_1$.

Before analysing the results of the evolution of this statistical quantities for all the ε values, we will qualitatively exemplify the dynamics of this ensembles only for $\varepsilon = 0.016$ and $\varepsilon = 0.020$.

We start with the smallest of these parameter values, using a *double section* technique applied by Lega *et al.* (2003) among others. While integrating the test particles we have taken the surface of section $x_1 = 0$ $(v_1 > 0)$ and asked whether the intersecting point also satisfies the condition $x_2^2 + x_3^2 \leq \delta^2$ $(v_2 > 0,\ v_3 > 0)$,

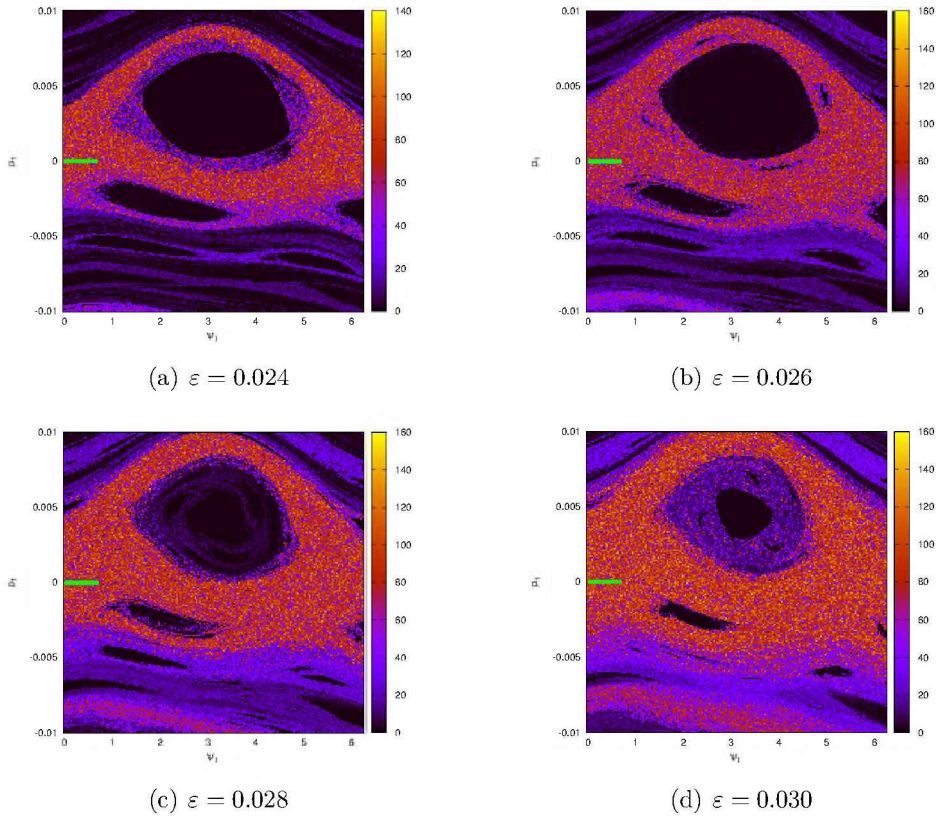

(a) $\varepsilon = 0.024$ (b) $\varepsilon = 0.026$

(c) $\varepsilon = 0.028$ (d) $\varepsilon = 0.030$

Figure 4. $\bar{Y}(3500 \times 2\pi)$, for $\varepsilon \in \{0.024,\ 0.026,\ 0.028,\ 0.030\}$, in a neighbourhood of $\boldsymbol{I}^r$ as given by Eq. (24), using pendulum variables (ψ_1, p_1). The green points identify the initial conditions of the ensembles.

with $\delta = 0.003$. In terms of angle variables the double section is equivalent to $\theta_1 = \pi/2$ with both θ_2 and θ_3 belonging to a certain neighbourhood (whose length decays to zero with δ) of $\pi/2$.

In Fig. 5 we plot all the intersections with the double section that have taken place since $t = 0$ up to five final times: $t = 10^5,\ 5 \times 10^5, 10^6,\ 5 \times 10^6, 10^7$. There we can see how the ensemble expands along the stochastic layer of the guiding resonance. Besides, for $t \geq 5 \times 10^6$, some of the particles are located on "stochastic filaments" that go across the oscillation domain of the resonance.

The location of the initial conditions is shown with a white cross. The fact that the ensemble at the initial time seems to be in the regular zone inside the resonance, is a purely projective effect because in this experiment the initial angle values used in the SALI map are different than the ones used in the initial conditions of the ensemble.

Now we shift towards the $\varepsilon = 0.020$ case, making snapshots of the projections of the ensemble positions onto the $[I_1, I_2]$ plane, without applying any surface of section method. For this reason, this snapshots will show particles projected onto regular regions.

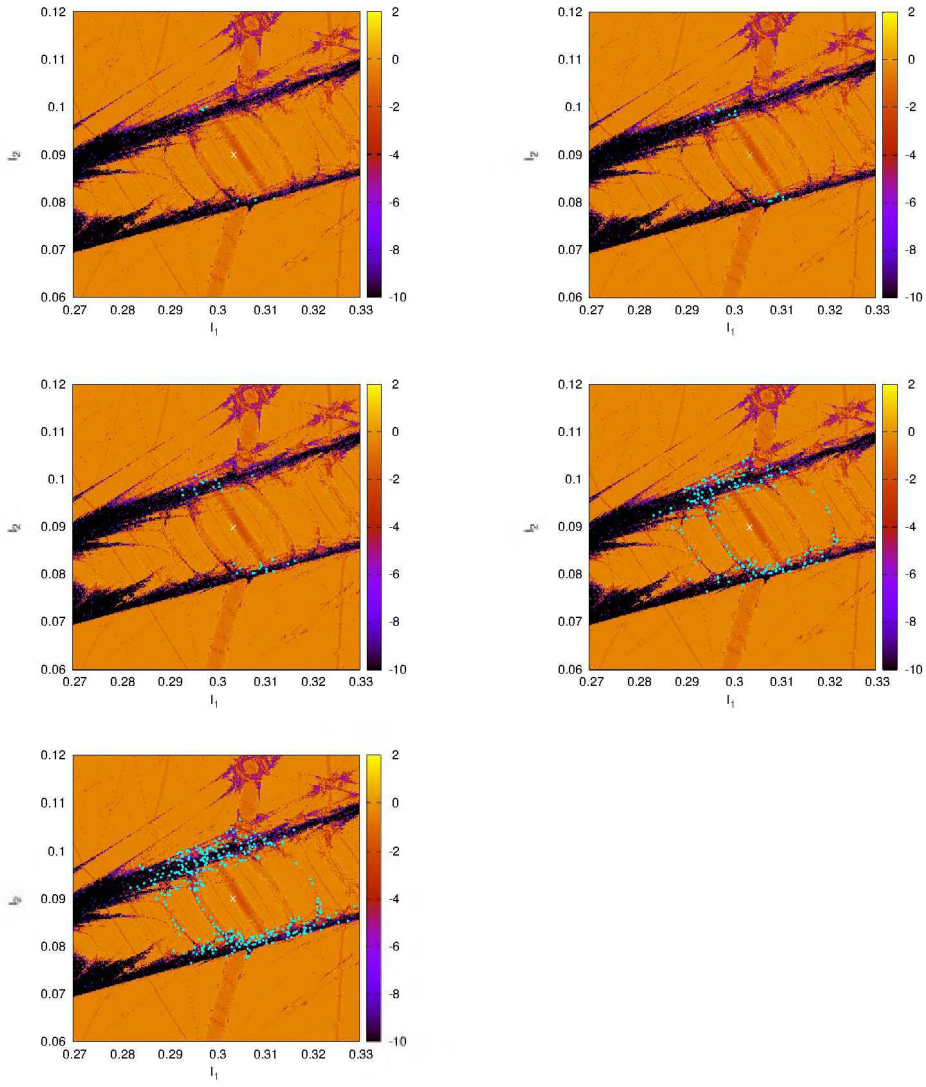

Figure 5. Intersection of the trajectories with the double section defined by $x_1 = 0$, $(x_2^2 + x_3^2)^{1/2} \leq 0.003$ and $v_i > 0$ $(i = 1, 2, 3)$, projected onto the $[I_1, I_2]$ plane for times: $t \leq 10^5$ (top–left), $t \leq 5 \times 10^5$ (top–right), $t \leq 10^6$ (middle–left), $t \leq 5 \times 10^6$ (middle–right) and $t \leq 10^7$ (bottom). The data corresponds to $\varepsilon = 0.016$.

In Fig. 6–left. we observe the situation of the ensembles for times $t = n \times 10^2$, with $n = 1, \ldots, 5$, in red, green, blue, magenta and yellow colors, respectively. Each point corresponds to a test particle (that appear overlapped due to their high density) and again, the location of the initial conditions is shown with a white cross. We observe mainly two phenomenae. One of them is an oscillatory behaviour of the centre of mass of an order of magnitude similar to the size of

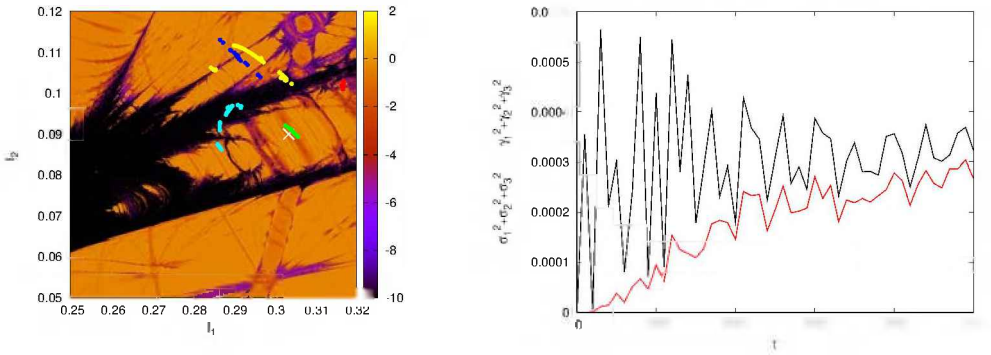

Figure 6. In the left hand side is displayed the location of the ensemble for times 0 (white cross), 10^2 (red), 2×10^2 (green), 3×10^2 (blue), 4×10^2 (cyan) and 5×10^2 (yellow) for $\varepsilon = 0.020$. In the right hand side is displayed $\sigma_*^2 \equiv \sigma_1^2 + \sigma_2^2 + \sigma_3^2$ (red) and $\gamma_*^2 \equiv \gamma_1^2 + \gamma_2^2 + \gamma_3^2$ (black), for $0 \leq t \leq 5 \times 10^3$ and the same ε value.

the resonance. The other one is a dispersion of the ensemble, related to the decorrelation of the resonant phases associated to the particles.

Both phenomenae can be quantified by observing at Fig. 6–right, where the evolution of the quantities $\sigma_*^2 \equiv \sigma_1^2 + \sigma_2^2 + \sigma_3^2$ (red) and $\gamma_*^2 \equiv \gamma_1^2 + \gamma_2^2 + \gamma_3^2$ (black), for the first 5×10^3 time units are shown.

The MSD presents oscillations. In particular, there is a peack of height approximately equal to 3.5×10^{-4} at $t = 100$. This implies that the distance of the ensemble with respect to the initial condition is of the order of $\gamma_* \approx (3.5 \times 10^{-4})^{1/2} \approx 0.019$, a fact that is verified graphically by the location of the red points in the snapshot.

On the other hand, the variance grows slower and with a more secular character than the MSD. Only after times $\gtrsim 2000$ the former quantity adquires values of the order of magnitude of the latter one. In the forthcoming diffusion measurements we will not consider this initial transient time.

The mentioned equivalence between these two quantities, for times outside the transient, can be appreciated in Fig. 7, where we give the positions of the particles for times of the form: $t = 3 \times 10^n$, with $n = 3, \ldots, 6$.

There it can be seen how the ensemble gradually expands. For times of the order of 10^3 (Fig. 7–top–left) the extension of the ensemble in the direction parallel to $\boldsymbol{\mu}_1$ is a bit larger that the one in the direction parallel to $\boldsymbol{\mu}_3$. Nevertheless, the situation is inverted when considering times of the order of 10^6 (Figs. 7–bottom–right), where there is evidence of a net macroscopic transport along the guiding resonance. A qualitatively similar situation was previously obtained for the $\varepsilon = 0.016$ case, in which the double section technique allowed a better visualization of the diffusion process in the action space. Fig. 8–left, shows the ensemble for 10^7 time units and gives evidence of the fact that there are particles that arrive close to the neighbouring resonances: $(2, -1, -1)$ and $(2, 0, -2)$. The $\sigma_*^2(t)$ y $\gamma_*^2(t)$ curves are displayed at Fig. 8–right for $0 \leq t \leq 10^7$. With the purpose of knowing the functional dependence of $\sigma_*^2(t)$, we assumed

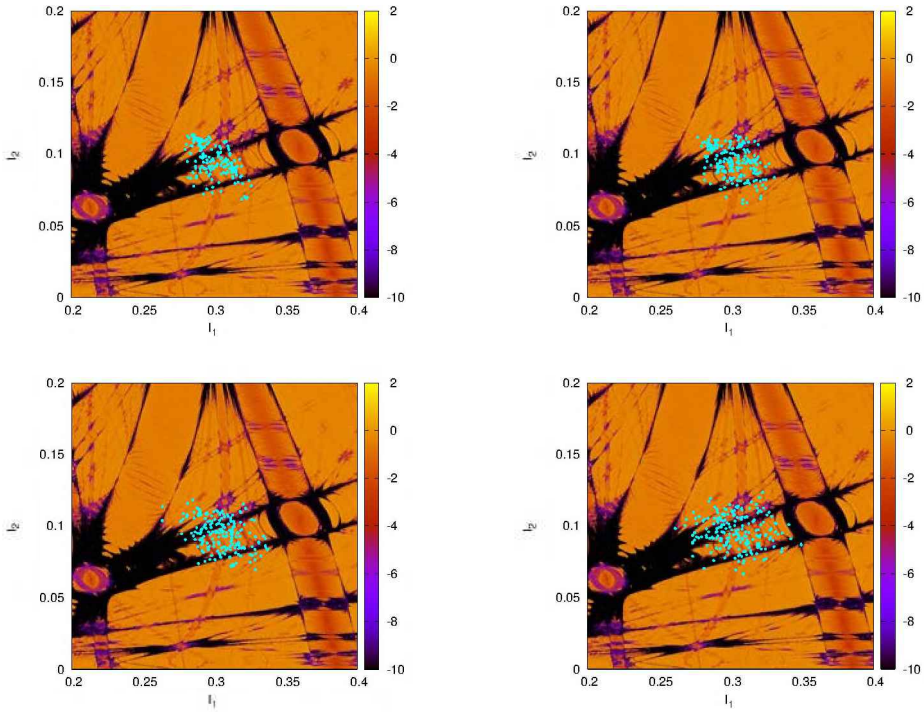

Figure 7. Ensemble projection onto the $[I_1, I_2]$ plane for times 3×10^3 (top–left), 3×10^4 (top–right), 3×10^5 (bottom–left) and 3×10^6 (bottom–right). The data corresponds to $\varepsilon = 0.020$.

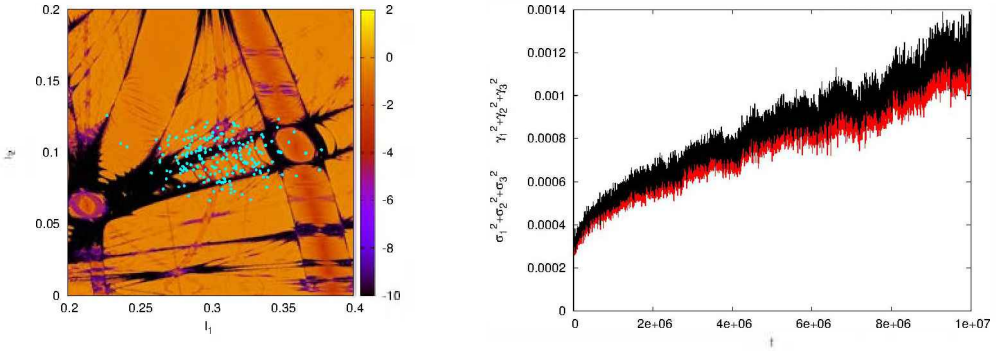

Figure 8. The left image shows a snapshot of the ensemble for $t = 10^7$ and $\varepsilon = 0.020$. The right image displays the curves of $\sigma_*^2 \equiv \sigma_1^2 + \sigma_2^2 + \sigma_3^2$ (red) and $\gamma_*^2 \equiv \gamma_1^2 + \gamma_2^2 + \gamma_3^2$ (black), for $0 \leq t \leq 10^7$ and the same parameter value.

as *ansatz* a power law:

$$\sigma_*^2 = \kappa t^w, \tag{27}$$

which is equivalent to the concomitant dependence of the FBM (21), associating w with the Hurst exponent according to $w = 2\eta$.

Applying the decimal logarithm to both sides of Eq. (27), we obtain

$$\log(\sigma_*^2) = \log(\kappa) + w \log(t).$$

This implies a linear relation between the logarithm of time and the logarithm of variance, being its slope the exponent of the power law. A numerical fit of the variables $\log(\kappa)$ and w, for $t \in [10^5, 10^{6.5}]$, gave that $\kappa \approx 2.23 \times 10^{-5}$ and that $w \approx 0.225$.

The fact that w turned out to be considerably smaller than unity, is an experimental evidence that during this time interval the diffusion is anomalous, and in particular, it is a subdiffusion process.

The length of this interval, that includes around 3×10^6 time units, is not negligible. On the contrary, observing Fig. 7–bottom–right, it can be stated that this time interval is a significant part of the life of the ensemble in which it is strictly included inside the guiding resonance, before that the particles arrive to the resonance crossings.

Fig. 9–left shows $\sigma_*^2(t)$ in logarithmic scale, together with the linear fit, while Fig. 9–right shows that this fit diverges from the real measurement, for larger times.

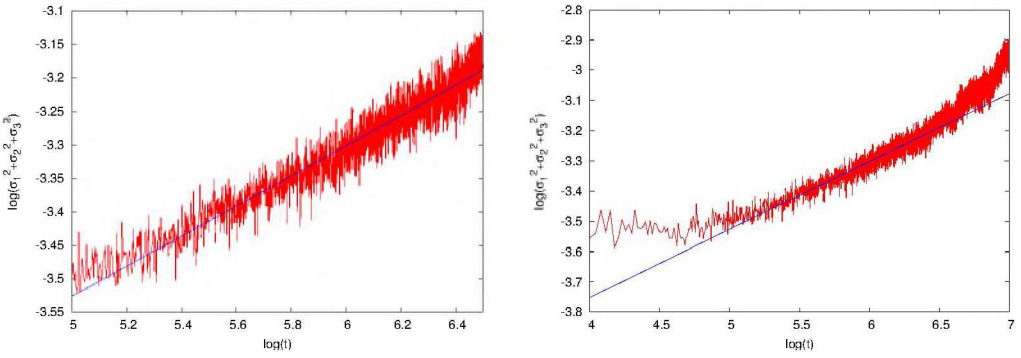

Figure 9. The left image displays $\log(\sigma_*^2)$ as a function of $\log(t)$ (red) together with the linear fit of the slope $w \approx 0.225$ (blue), for $t \in [10^5, 10^{6.5}]$. The right image shows that this power law behaviour ($\sigma_*^2 \propto t^w$) stops being valid when considering a wider time interval.

Now we will consider the evolution of the variances associated to each direction individually. Fig. (10) displays the curves $\sigma_1^2(t)$, $\sigma_2^2(t)$ and $\sigma_3^2(t)$ in colors red, green and blue, respectively, for $t \in [10^5, 10^7]$. We observe an approximate stabilization in constant values of σ_1^2 and σ_2^2, while σ_3^2 shows sustained growth. The stabilization of σ_2^2 is due to the conservation of the total energy. The stabilization of σ_1^2 is due to the fact that the resonant moment (p_1) is bounded due to the (aproximate and local) conservation of the energy of the resonant normal form, i.e. conservation of energy of the pendulum.

This behaviour of the variances is the one that should take place in an Arnold diffusion process (subsection 1.4.), during the stage in which the ensemble

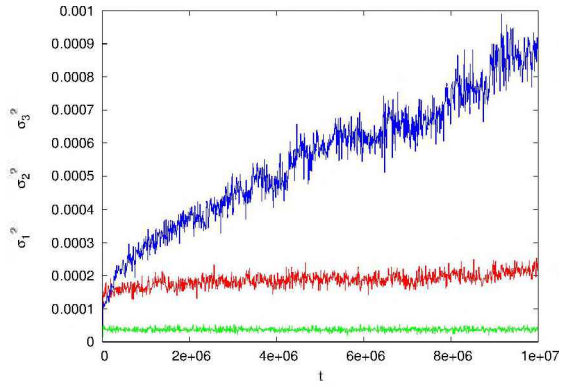

Figure 10. $\sigma_1^2(t)$, $\sigma_2^2(t)$ and $\sigma_3^2(t)$ respectively in red, green and blue colors, for $\varepsilon = 0.020$.

is mostly located inside the stochastic layer of the original guiding resonance. Once diffusion has proceeded considerably along other resonances, Chirikov's base associated to the original guiding resonance stops having geometrical sense. When particles change their guiding resonance, there is a change in $\boldsymbol{\mu}_1$ and $\boldsymbol{\mu}_3$ as they both depend on $\boldsymbol{m}_g$; and there is a change in $\boldsymbol{\mu}_2$ due to the convexity of $\mathcal{I}_0$.

Fig. 11 displays the values of the three variances for each value of $\mathscr{E}$.

There it can be seen the change in the behaviour of variances as the intensity of the perturbation gradually increases. Figs. 11 (a,b,c) show that for $\varepsilon \in \{0.016,\ 0.018\}$ the behaviour is qualitatively similar to the one previously described for $\varepsilon = 0.020$.

Figs. 11 (d,e,f) show that for $\varepsilon \in \{0.022,\ 0.024,\ 0.026\}$, σ_1^2 does not stabilize, but it has a net growth. On the other hand, σ_2^2 still converges approximately to a constant value, while σ_3^2 is still the variance that grows largely in the analysed time interval.

Finally, in Figs. 11 (g,h) there is evidence of the fact that for $\varepsilon \in \{0.028,\ 0.030\}$, σ_2^2 presents a net growth and, besides, the magnitude of the growth of σ_1^2 is of the order of the one of σ_3^2. This behaviour does not agree with an Arnold diffusion at all. Therefore, for $\varepsilon = 0.028$, which is smaller than ε_c (section 2.), there is a diffusion situation geometrically more similar to an *overlapping regime* than to an Arnold diffusion.

Nevertheless, there is no contradiction in these facts because the quantity ε_c gives information of the global state of overlap of phase space, while in the local neighbourhood of our particular resonant action under study, the overlapping starts to manifest for smaller values of ε.

This argument can be experimentally proved by considering the two bottom images of Fig. 4, that show that for values of ε equal to 0.028 and 0.030, the resonant region is in an advanced state of overlap.

Once that we have analysed the way in which the variances (associated to the three independent directions of Chirikov's base) change with respect to ε, we will go ahead towards quantitative measurements of the evolution of only one of the variances: σ_3^2.

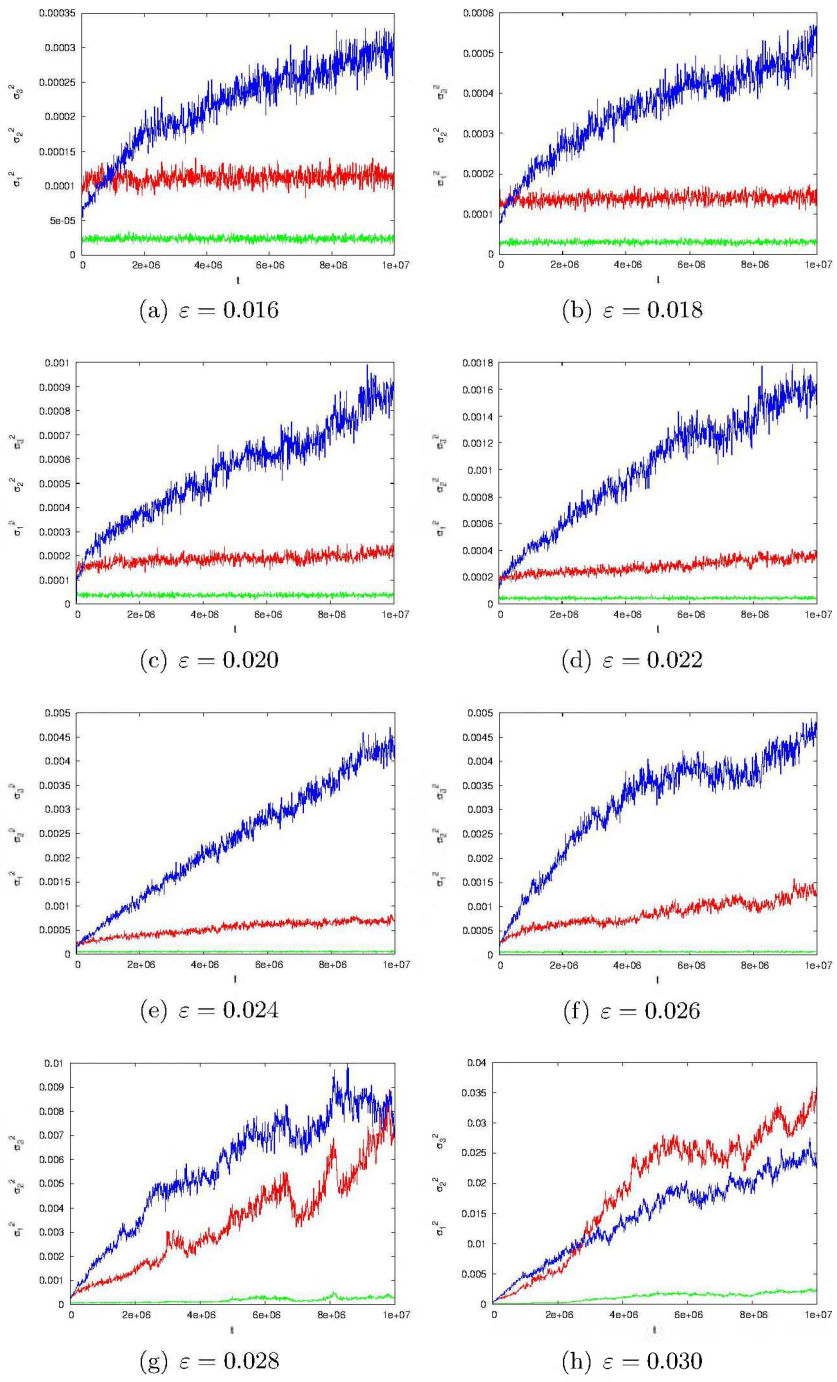

(a) $\varepsilon = 0.016$ (b) $\varepsilon = 0.018$

(c) $\varepsilon = 0.020$ (d) $\varepsilon = 0.022$

(e) $\varepsilon = 0.024$ (f) $\varepsilon = 0.026$

(g) $\varepsilon = 0.028$ (h) $\varepsilon = 0.030$

Figure 11. $\sigma_i^2(t)$ $(i = 1, 2, 3)$ respectively in red, green and blue colors, for $\varepsilon \in \mathscr{E}$.

Fig. 12–left shows $\sigma_3^2(t)$ in logarithmic scale for $\varepsilon \in \mathscr{E}$, in colors red, green, blue, magenta, cyan, yellow, black and orange, respectively. We observe that, in general, for each fixed time t, the larger the value of ε, the larger the value of $\sigma_3^2(t)$. For each curve, we have made a linear fit for $t \in [10^5, 10^{6.5}]$, proceeding in a similar way to what had previously been done with σ_*^2 and Eq. (27).

Table 1 displays the values of this numerical fits. In the fifth column the quantity w_* has been added, which corresponds to a fitted value of the exponent for a wider time interval, $t \in [10^5, 10^7]$, while the sixth column shows the concomitant percentage relative difference. It can be seen that for some values of ε, such a difference reaches values higher than 15%. This is an example of the fact that the behaviour of statistical quantities in systems with divided phase space can be highly dependent on the size of the time interval.

Fig. 12–right shows the agreement between the linear fit done in $10^5 \leq t \leq 10^{6.5}$ and the concomitant evolutions of variances. Analogously, Fig. 13–left displays the same information for the range $10^5 \leq t \leq 10^7$. Fig. 13–right shows the values of both exponents, w and w_*, as a function of ε in red and black colors, respectively.

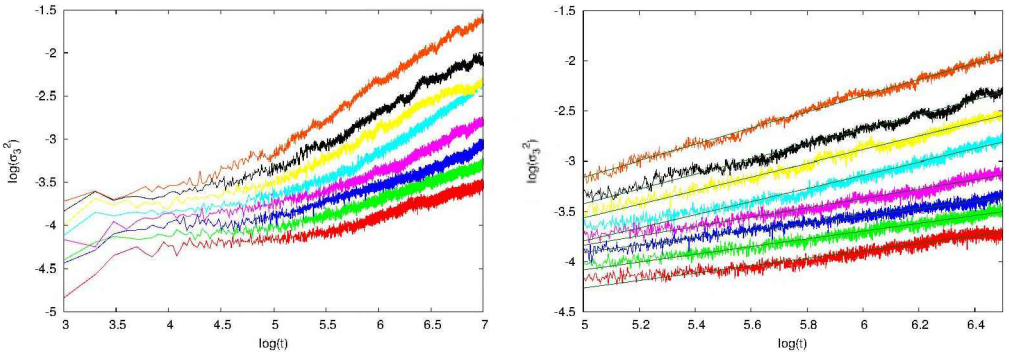

Figure 12. $\sigma_3^2(t)$ in logarithmic scale, for $\varepsilon \in \mathscr{E}$, in colors red, green, blue, magenta, cyan, yellow, black and orange, respectively. In the left hand side image the time range is $t \in [10^3, 10^7]$. In the right hand side image, the concomitant straight lines that fit approximately the data for $t \in [10^5, 10^{6.5}]$ have been added.

Due to the fact that every measured value of w (and of w_*) is less than unity, it can be concluded that for the two temporal ranges, and for the eight ε values analysed, the variance evolution corresponds to an anomalous diffusion process of the subdiffusive type.

Therefore, having also in mind the information obtained from Figs. 11 (a,b,c), it could be said that for $\varepsilon \in \{0.016,\ 0.018,\ 0.020\}$ and for the two time ranges used, an "Arnold subdiffusion" process might be taking place.

In spite of this, Fig. 14 indicates that when considering times sufficiently shorter than the ones recently used, the variances follow an approximately linear behaviour. In order to have an estimation of the average rate of change of the variance during the earliest 5×10^5 time units, we will compute the diffusion coefficient $\mathcal{D}_\sigma$ (20), choosing as initial time $t_0 = 10^4$ and as final time $t = 5 \times 10^5$.

ε	w	$\log(\kappa)$	κ	w_*	$\frac{\lvert w-w_*\rvert}{w} \times 100$
0.016	0.370366	−6.11277	7.713×10^{-7}	0.365061	$\sim$ 1
0.018	0.387073	−6.01603	9.638×10^{-7}	0.395128	$\sim$ 2
0.020	0.363961	−5.72554	1.881×10^{-6}	0.444984	$\sim$ 22
0.022	0.466993	−6.17054	6.752×10^{-7}	0.564104	$\sim$ 20
0.024	0.654695	−7.06677	8.575×10^{-8}	0.755714	$\sim$ 15
0.026	0.676915	−6.94744	1.129×10^{-7}	0.562896	$\sim$ 16
0.028	0.736347	−7.10383	7.874×10^{-8}	0.655036	$\sim$ 11
0.030	0.807722	−7.19636	6.363×10^{-8}	0.756279	$\sim$ 6

Table 1. Results of the numerical fit of the power law, similar to the ansatz given by Eq. (27), with the substitution of σ_* with σ_3, for $t \in [10^5, 10^{6.5}]$. In the fifth column the quantity w_* has been added, which corresponds to a fitted value of the exponent for a wider time interval, $t \in [10^5, 10^7]$, while the sixth column shows the concomitant percentage relative difference.

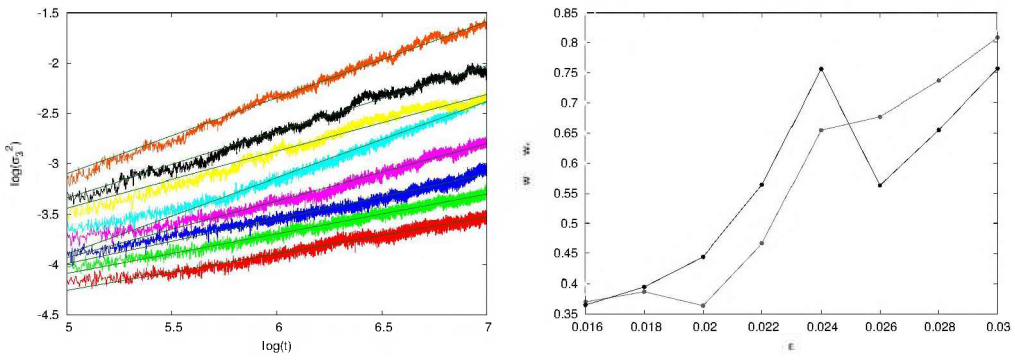

Figure 13. The left hand side image shows the curves $\sigma_3^2(t)$ in logarithmic scale, for $\varepsilon \in \mathscr{E}$, in colors red, green, blue, magenta, cyan, yellow, black and orange, respectively, together with the concomitant straight lines that fit approximately the data, for $t \in [10^5, 10^7]$. The right hand side image shows the $w(\varepsilon)$ and $w_*(\varepsilon)$ curves in red and black colors, respectively.

This information is provided by Table 2 and by Fig. 15, as a function of ε. Looking at this figure it is not possible to determine the functional relation between the diffusion coefficient and the perturbative parameter. Due to the smallness of the ε–range used, the data could be compatible with many functional forms. Nevertheless, it is noticeable that $\mathcal{D}_\sigma$ increases when ε increases, as expected.

4. Conclusion

In this work we have studied, through numerical experiments, a diffusion process that takes place along the stochastic layer of a guiding resonance of a particular *quasi*–integrable 3DoF Hamiltonian flow.

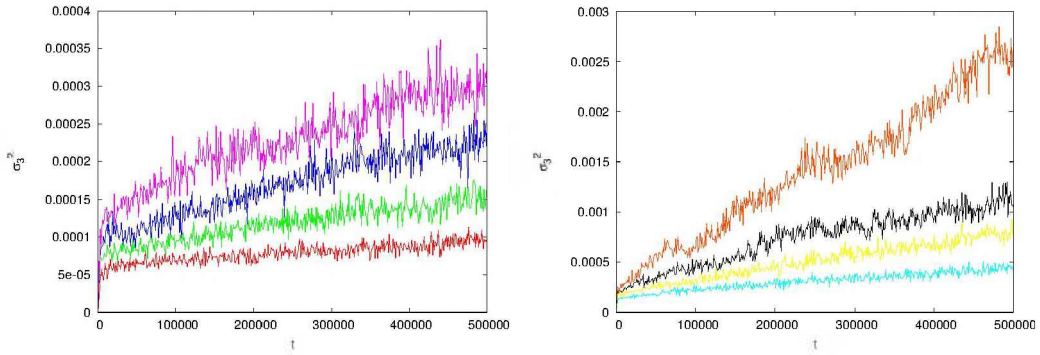

Figure 14. $\sigma_3^2(t)$ for $\varepsilon \in \mathscr{E}$ and $t \leq 5 \times 10^5$. Each color corresponds to an ε value, following the same criterion of Fig. 12.

ε	$\sigma_3^2(t_0)$	$\sigma_3^2(t)$	$\mathcal{D}_\sigma$
0.016	0.571×10^{-4}	0.102×10^{-3}	4.59×10^{-11}
0.018	0.739×10^{-4}	0.162×10^{-3}	9.01×10^{-11}
0.020	0.107×10^{-3}	0.208×10^{-3}	1.02×10^{-10}
0.022	0.136×10^{-3}	0.265×10^{-3}	1.31×10^{-10}
0.024	0.140×10^{-3}	0.414×10^{-3}	2.78×10^{-10}
0.026	0.153×10^{-3}	0.839×10^{-3}	6.99×10^{-10}
0.028	0.237×10^{-3}	0.105×10^{-2}	8.30×10^{-10}
0.030	0.288×10^{-3}	0.261×10^{-2}	2.37×10^{-9}

Table 2. $\mathcal{D}_\sigma(\varepsilon)$, using $t_0 = 10^4$ and $t = 5 \times 10^5$.

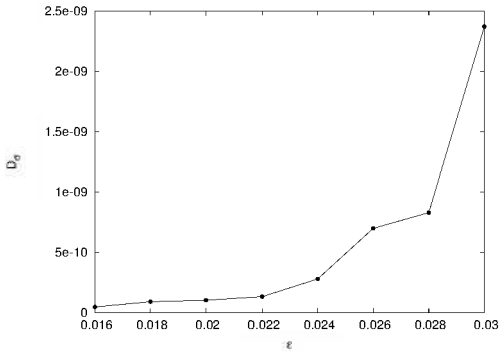

Figure 15. $\mathcal{D}_\sigma(\varepsilon)$, using $t_0 = 10^4$ and $t = 5 \times 10^5$.

We have considered eight values of the perturbation parameter (ε). For each one of these values we have used an ensemble of test particles whose initial conditions were chosen inside the stochastic layer of the perturbed guiding resonance.

We have measured the evolution of the variances and mean square displacements, in the three directions of Chirikov's base, determining that for $\varepsilon \leq 0.02$

the results geometrically agree with an Arnold diffusion. Such a process is characterized by the fact that $\sigma_1^2(t)$ and $\sigma_2^2(t)$ stabilize around constant values, while $\sigma_3^2(t)$ performs a nearly secular growth in the time interval under analys: $t \in [0, 10^7]$.

For higher ε values, we have found that $\sigma_1^2(t)$ has an average growth rate that increases with ε, in agreement with the fact that the degree of influence of the overlap with neighbouring resonances increases with ε.

For $t \lesssim 10^7$ we have observed an anomalous behaviour of $\sigma_3^2(t)$ for all the eight ε values. Through numerical fits of $\sigma_3^2(t)$, of the power law type, we have found that all the exponents are lower than one, In other words, all the Hurst exponents are lower than one half. This is experimental evidence of the existence of a subdiffusion process that *effectively* takes place in this given time interval.

On the other hand, for $t \lesssim 5 \times 10^5$ we have observed that these variances behave approximately linearly (normal diffusion). This allowed us to compute diffusion coefficients, $\mathcal{D}_\sigma$, associated to the rate of growth of the variances. We have found that $\mathcal{D}_\sigma$ increases with ε.

Acknowledgments. This work was supported with grants from the Consejo de Investigaciones Científicas y Técnicas de la República Argentina, and the Universidad Nacional de La Plata. We thank the anonymous referee for the comments and for suggesting the implementation of the double section technique.

References

Arnold, L. 1973, Stochastic Differential Equations: theory and applications

Arnold, V. I. 1989, Mathematical Methods of Classical Mechanics

Bazzani, A., Beccaceci, L., Bigliardi, L., & Turchetti, G. 1997, American Institute of Physics Conference Series, 395, 109

Bazzani, A., & Mais, H. 1998, Nonlinear and stochastic beam dynamics in accelerators - A chalenge to theoretical and computational physics, 74

Bountis, T., & Kollmann, M. 1994, Physica D, 71, 122

Chechkin, A. V., Metzler, R., Klafter, J., & Gonchar, V. Y. 2008, Anomalous Transport, 129

Chirikov, B. V. 1979, Phys. Rep, 52, 263

Cincotta, P. M. 2002, New Astron. Rev, 46, 13

Cincotta, P. M., Giordano, C. M., & Simó, C. 2003, Physica D, 182, 151

Cincotta, P. M., & Simó, C. 2000, A&AS, 147, 205

Cordeiro, R. R. 2006, AJ, 132, 2114

Cordeiro, R. R., & Mendes de Souza, L. A. 2005, A&A, 439, 375

Efthymiopoulos, C. 2008, Celest. Mech. Dyn. Astron, 102, 49

Einstein, A. 1956, Annalen der Physik (Leipzig), 17, 549

Froeschlé, C., Guzzo, M., & Lega, E. 2005, Celest. Mech. Dyn. Astron, 92, 243

Gardiner, P. R. 2004, Handbook of Stochastic Methods

Giordano, C. M. & Cincotta, P. M. 2004, A&A423, 745

Gradshtyn, I. S., & Ryzhik, I. M. 1980, Table of Integrals, Series and Products

Guzzo, M., Lega, E., & Froeschlé, C. 2005, Disc. Cont. Dyn. Syst. B, 5, 687

Lega, E., Guzzo, M., & Froeschlé, C. 2003, Physica D, 182, 179

Mandelbrot, B. B. & van Ness, J. W. 1968, SIAM Review, 10, 422

Mestre, M., Cincotta, P. M., & Giordano, C. M. 2009, Int. J. Nonlinear Mech, 44, 180
Metzler, R., Chechkin, A. V., Klafter, J. 2007, ArXiv e-print
Morbidelli, A. 2006, Modern Celestian Mechanics – Aspects of Solar System Dynamics
Nekhoroshev, N. N. 1977, Russ. Math. Surv, 32, 1
Novaković, B., Tsiganis, K., & Knežević, Z. 2010, MNRAS, 402, 1263
Prince, P. J., & Dormand, J. R. 1981, J. Comput. Appl. Math, 7–1, 67
Schlier, C. & Seiter, A. 2000, Comput. Phys. Commun, 130, 176
Siboni, S., Turchetti, G., Vaienti, S. 1994, J. Stat. Phys, 75, 167
Skokos, C. 2001, J. Phys. A – Math. Gen, 34, 10029
Todorović, N., Lega, E., & Froeschlé, C. 2008, Celest. Mech. Dyn. Astron, 102, 13
Zaslavsky, G. M. 2002, Phys. Rep, 371, 461